IEEE Photonics Journal
An IEEE Photonics Society Publication

Open Access

Optofluidic Planar Optical Cross-Connect Using Nematic Liquid-Crystal Waveguides

Volume 10, Number 04, August 2018

Tenghao Li
Qingming Chen
Xuming Zhang

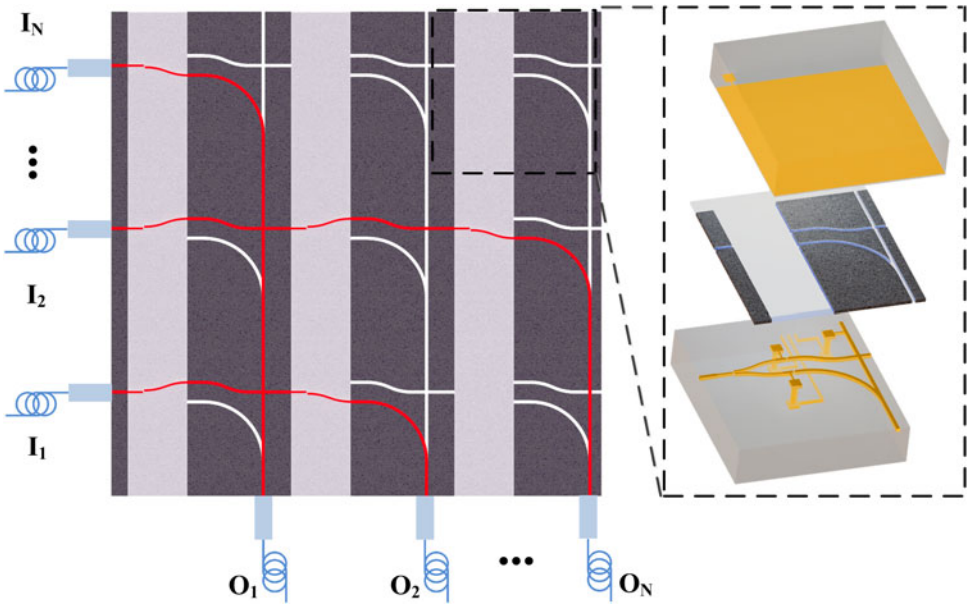

DOI: 10.1109/JPHOT.2018.2853759
1943-0655 © 2018 IEEE

IEEE photonics SOCIETY

IEEE

Optofluidic Planar Optical Cross-Connect Using Nematic Liquid-Crystal Waveguides

Tenghao Li,[1] **Qingming Chen**,[1] **and Xuming Zhang** [1]

[1]Department of Applied Physics, The Hong Kong Polytechnic University, Hong Kong

DOI:10.1109/JPHOT.2018.2853759

Manuscript received June 2, 2018; revised June 29, 2018; accepted July 4, 2018. Date of publication July 31, 2018; date of current version August 2, 2018. This work was supported by the Research Grants Council of Hong Kong through the General Research Fund (N_PolyU505/13, PolyU 5334/12E, PolyU 152184/15E and PolyU 152127/17E), by Hong Kong Polytechnic University (G-YN07, G-YBBE, G-YBPR, 4-BCAL, 1-ZVAW, 1-ZE14, A-PM21, 1-ZE27 and 1-ZVGH), and by the National Science Foundation of China (no. 61377068). Corresponding author: Xuming Zhang (apzhang@polyu.edu.hk).

Abstract: This paper proposes a compact planar optofluidic optical cross-connect (OXC) switch based on electro-optic (EO) waveguides in nematic liquid crystal (NLC). In the cross-bar fabric, each unit cell of the proposed device consists of two portions: the NLC EO waveguides for 1 × 2 switching and the fixed NLC-core waveguides to support subsequent beam paths of the lead-in/lead-out process or the bending process. With numerical simulations, a sample design of 8 × 8 OXC is analyzed and optimized, which provides the predicted broadband performance as approximately 8.0 dB maximum on-chip insertion loss, –45.9 dB cross-talk and 16 ms switching time in the footprint of 2 mm × 2 mm. The loss reduction and the switching speed-up issues are also discussed, with the expected 5.5 dB maximum on-chip insertion loss and 1 ms switching time. The proposed OXC switch is new in the working principle using both electric-field reconfigurable NLC waveguides and fixed NLC-core waveguides, and can leverage the liquid-crystal on silicon fabrication. It is potential for optical circuit switching in the small-scale data centers, or protection switching in optical communication networks.

Index Terms: Liquid-crystal devices, optical switching, integrated photonics.

1. Introduction

The rapid development of Internet applications such as mobile communication, high-definition video and cloud-based computing [1] has urged an explosive rise of data traffic, which demands more data centers with larger capacity and faster processing. Many research efforts have been devoted to incorporating optical cross-connect (OXC) into future data centers [1]–[3] to avoid the optical-electronic-optical (OEO) conversion, which has long been the bottleneck of data communications [4].

A variety of OXC techniques for data centers and optical communication have been proposed and developed, including free-space OXCs based on micro-electro-mechanical systems (MEMS) [5] and liquid crystal on silicon (LCoS) [6], semiconductor optical amplifier (SOA) based optical switches [7], silicon optical switches [8], MEMS silicon photonics switches [9], and so on. Fast optical packet switching is constantly under exploration [10], [11], but most of the practical techniques are still based on optical circuit switching with relatively slow switching ranging from several microseconds to tens of milliseconds [1]–[11]. In general, the free-space OXCs support large port amount but

suffer from bulk size and complicated optical alignment. The silicon optical switch with the switch-and-selector architecture [8] provides a solution of 8 $\times$ 8 ports, low loss and compact size, but it has the difficulty in scaling up for more ports. The MEMS silicon photonic switch supports a monolithic integration with 50 $\times$ 50 ports and around 24 dB maximum optical loss [9]. However, the MEMS devices generally require strict control of environment factors (such as temperature and humidity) to maintain the robustness and durability [12]. In contrast, the LCoS switches usually have good scalability and high robustness, thanks to no moving mechanical parts [13]. The SOA-based switch can provide fast response and easy integration, but often consumes more power in the current-driven scheme [10].

The development on optofluidic OXC can date back to 1990s, with the report of bubble-type OXC based on air-bubble controlled planar-silica-waveguide cross-points [4]. An optofluidic switch was also proposed in recent year [14] which is based on the micro-ring resonator driven by digital microfluidics, though with limited working bandwidth. As for special working material of liquid crystal (LC), the nematic liquid crystal (NLC) device was reported using tunable total-internal reflection (TIR) interfaces in the NLC trenches [4]. However, the requirement of high surface quality in the trench and the limited refractive index (RI) contrast pose critical limitations to practical TIR NLC devices. As a member of the family of field-induced waveguide (FIG) [15], the electro-optic (EO) waveguides remain under exploration by using NLC in recent years [16]–[19]. For instance, the multimode NLC waveguide and the corresponding 1 $\times$ 2 switching were experimentally studied using the LC layer of 30 μm thick and the patterned alignment in assembly [16]. The isotropic/para-nematic phase LC waveguides were proposed and fabricated [17]–[19] for the applications of optical switches [17], optical variable attenuators [18] and beam splitters [19]. Although the isotropic phase LCs can be used in the EO waveguides to shorten the switching time to the order of microseconds, their small EO coefficient results in high driving voltage and large footprint as compared to the NLC devices [20], making it generally difficult to realize integrated OXCs. The low-loss NLC-core waveguides have been experimentally studied in recent years [21]–[23], though limited to the main application as tunable attenuators. The distributed feedback gratings [24] and the plasmonic optical switches [25] using the NLC waveguides were also proposed and analyzed recently. There is still plenty of room to design compact planar OXCs based on the NLC.

In this paper, a planar optofluidic OXC solution will be presented and analyzed based on NLC waveguides (named as NLC-OXC). The NLC-OXC consists of an array of planar unit cells that are connected and switched by the NLC EO waveguides and the fixed NLC-core waveguides, which is different from the previous reported devices [16], [17] where only LC EO waveguides are applied. With the fixed NLC-core waveguides, the NLC-OXC can support low-loss 90-degree bending with small radius ($\sim$100 μm), and thus allows better integration and performance in an array of switching units. By leveraging the LCoS fabrication technique, it can further combine the advantages in the compactness of planar waveguide, the robustness of LCoS, and the requirement of low driving voltage due to the use of NLC.

2. Concept and Scheme

The scheme of NLC-OXC is presented in Fig. 1(a), using a 3 $\times$ 3 array as the example for easy illustration. It is noted that this scheme is not limited to 3 $\times$ 3 array but can be used generally for more port counts. The light beams are injected into the input ports (e.g., I1, I2 and I3 in Fig. 1(a)). They are then switched and delivered separately to the output ports (e.g., O1, O2 and O3 in Fig. 1(a)). In each unit cell, the light beams (the red lines in Fig. 1(a)) can be either conveyed forward, or bended into the perpendicular direction.

As shown in Fig. 1(b), the unit cell consists of three functional layers, the top cladding layer, the chamber layer and the bottom cladding layer. The top cladding layer is coated with a thin metal (or transparent conductive oxide) layer and acts also as the common electrical ground in addition to the optical cladding function in the vertical direction. The chamber layer is made of polymer and has patterned chambers and channels for the filling of NLC. The bottom cladding layer is patterned with metal electrodes, which can work under high voltage to drive the rotation of NLC.

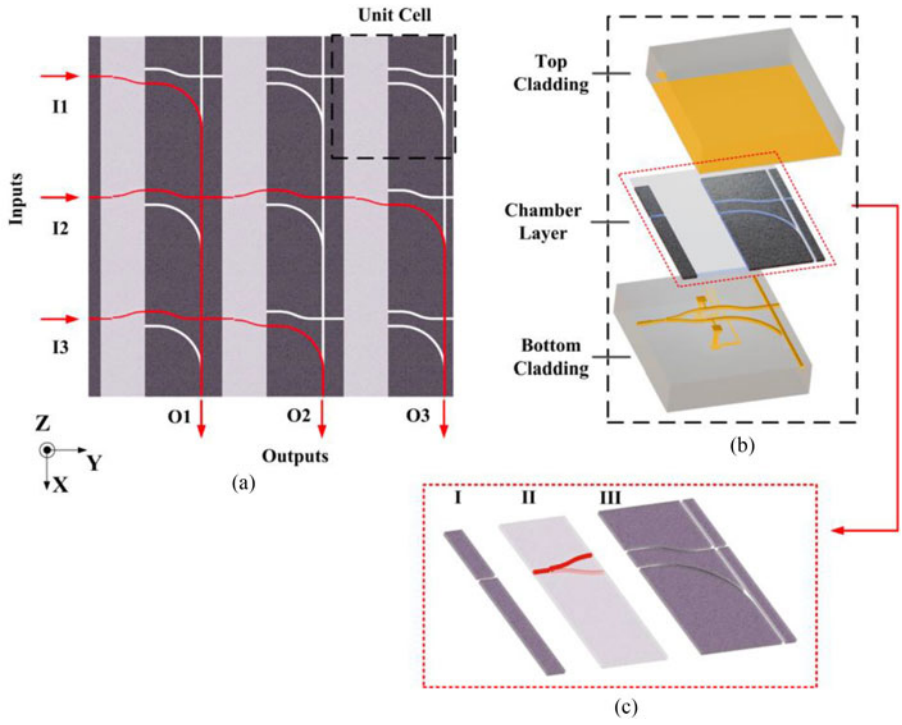

Fig. 1. The proposed scheme of NLC-OXC is sketched, with (a) top view of the NLC-OXC; (b) thee layers of a unit cell; and (c) the functional portions for light propagation.

Fig. 1(c) shows more details of the chamber layer, each unit cell can be divided into two portions along the direction of light propagation, including the NLC-core waveguide element (I, and III in Fig. 1(c)) and the 1 $\times$ 2 switching element (II in Fig. 1(c)). The NLC-core waveguides provide the fixed light propagation paths while the 1 $\times$ 2 switching element is the key component to select the propagation direction. For the NLC-core waveguides, the channels are surrounded by polymer. The filled NLC driven by an operating voltage forms the waveguide core, while the polymer with a lower RI acts as the cladding. In contrast, the 1 $\times$ 2 switching element is composed of the NLC only, and the EO waveguides are turned on/off by applying the high/zero operating voltage to the corresponding electrodes on the bottom cladding layers.

It is important to combine both the NLC EO waveguides and the fixed NLC-core waveguides in the proposed design. The NLC EO waveguide can provide configurability under electric field with simple structure. However, in the case of waveguide bending, it also suffers from unbearable light leakage even for large radius up to $\sim$mm [16]. It is a fundamental defect, since the unavoidable fringing effect [26] induce the gradient variation of NLC directors at the bending's inner and outer boundaries, and the propagating light is polarization-rotated when it strikes at the boundaries. The shift of mode field towards the outer edge [27] further strengthens this kind of leakage. Especially when there is a large-angle bending (e.g., 90° bending), almost all the light power escapes in the form of the other polarizations, and the small-radius ($<$1 mm) bends are generally precluded. If the isotropic phase LC waveguide is applied instead, such strong light leakage can be totally removed in principle, but at the cost of large footprint because of the low RI contrast [17]. As a solution, the fixed NLC-core waveguides are implemented to support 90-degree bending instead of the NLC EO waveguides.

The three processes for the light propagation are then shown in Fig. 2, including the lead-in process (red in Fig. 2(a)), the lead-out process (green in Fig. 2(a)) and the bending process (red in Fig. 2(b)). In the lead-in process, the light propagates from the previous unit cell (e.g., part I in

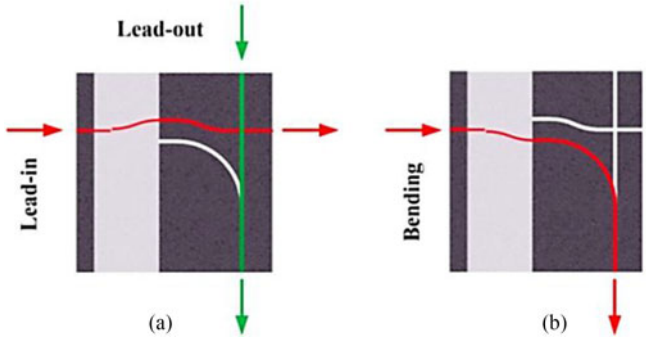

Fig. 2. Working states of the unit cell. (a) Bar state, which accommodates the lead-in process (red) and the lead-out (green) at the same time; and (b) the cross state, as realized by the bending process (red).

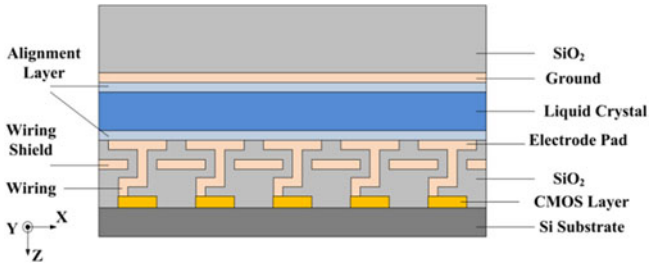

Fig. 3. Cross-sectional view of the layers of the NLC-OXC is presented.

Fig. 1(c)) to the current one (e.g., part III in Fig. 1(c))) through the 1 $\times$ 2 switching element. In the lead-out process, the light stays in the NLC-core waveguides and propagates downward to the output port, encountering several waveguide crossings. Similarly, the bending process is realized by connecting the lead-in waveguide and the 90-degree bending through 1 $\times$ 2 switching. In terms of the unit cell's working states, the lead-in process and the lead-out process correspond to the bar state and can be obtained at the same time, whereas the bending process corresponds to the cross state. These enable the non-blocking switching of each unit cell and thus the whole OXC device.

3. Device Design

The design of the sample device is presented in this section, which mainly covers the layered structure, the patterned electrodes, the channel structures, and also the material choices.

The transverse cross-section view of the layered structure is illustrated in Fig. 3, showing seven layers in total. Similar to the LCoS [29], [30], the bottom layer of the NLC-OXC is the CMOS layer deposited on the silicon substrate. A patterned electrode layer is further fabricated on the CMOS layer, with aluminum wires buried in the SiO_2 insulator for electrical connections in the vertical direction. In addition, a wiring shield is formed around the electrical vias to improve the electrical performance. The chamber layer for the NLC is directly sandwiched by alignment layers on both sides. As mentioned above, the chamber layer is patterned in the NLC-core waveguide element and is open in the region of 1 $\times$ 2 switching element. In the sample design, the NLC is chosen to use E7 by Merck [24]. The planar alignment [28] is realized by anchoring the NLC on the SiO_x surface [31], [32]. The SiO_x thin film can be fabricated by the thermal evaporation method [32], without the need for rubbing process. By controlling the evaporation direction, the NLC molecules are pre-aligned to make their directors parallel to the Y direction everywhere as shown in Fig. 3.

The thickness of both alignment layers is 100 nm [31]. The thickness of the electrodes is designed to be 100 nm as well. In Fig. 3, the NLC chamber thickness T_{LC} is the critical parameter since it

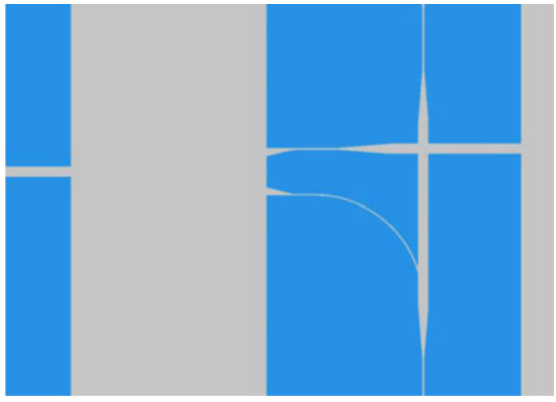

Fig. 4. The pattern of the NLC-core waveguide is presented. The blue portion stands for the polymer, the grey one for the channel of LC.

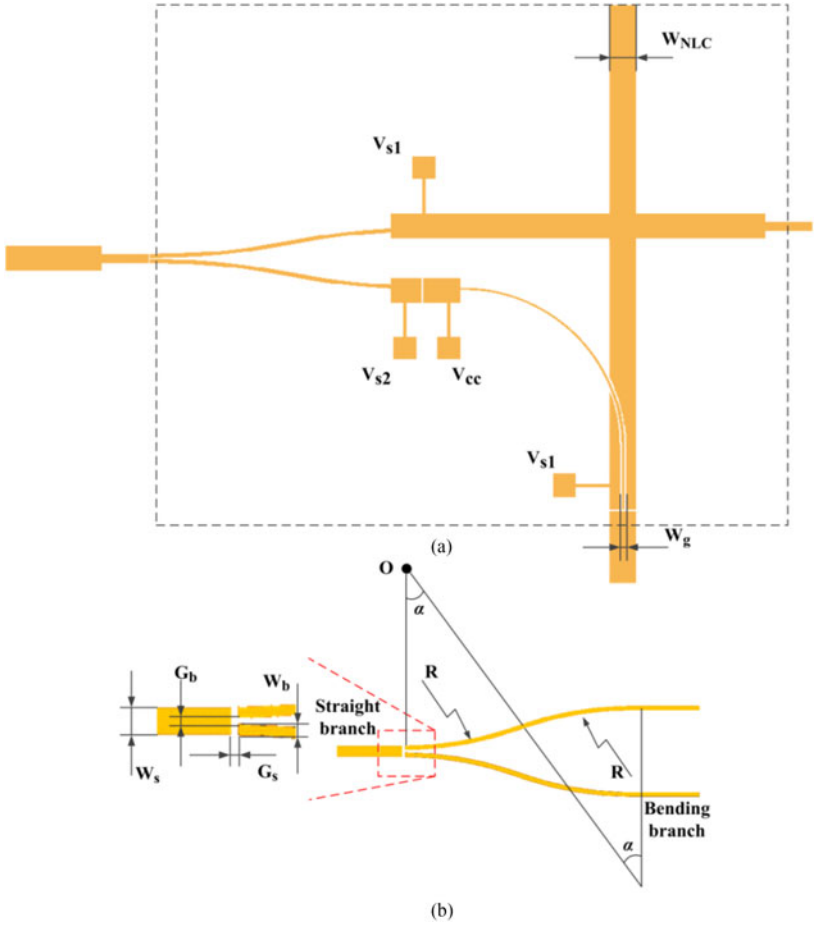

Fig. 5. The pattern of the electrodes is shown, including (a) the overall pattern, and (b) the pattern in the 1 × 2 switching element. The golden color stands for the electrodes.

determines the waveguide modes, the switching speed of NLC and the required driving voltage. Because of the gradient index property in NLC waveguide, the CMOS layer has little influence on the light propagation and is thus neglected, with only the topmost electrode pads considered in the following design and analysis.

TABLE 1
Main Structure Parameters of the NLC-core Waveguide Element

Parameters	Value
Channel width W_C	5 μm
Bending channel width $W_{C,b}$	1 μm
Bending channel radius R_b	50 μm
Length of lead-in waveguide $L_{lead\text{-}in}$	90 μm
Length of lead-out waveguide $L_{lead\text{-}out}$	165 μm
Length of bending waveguide L_{bend}	200 μm

In the specific example, the designs of the NLC-core waveguide structures and the patterned electrodes are further depicted in Figs. 4 and 5, respectively. The pattern of the polymer channel (the blue one in Fig. 4) defines the beam path in the NLC-core waveguide portion. Waveguide tapers [33] are used to connect the EO waveguides and the NLC-core waveguides, or the narrow waveguides and the wide ones in the NLC-core waveguide element. The narrow waveguides with the width of 1 μm are applied to reshape the mode field to the fundamental mode, or to maintain it at the waveguide bends. Wider waveguides with the width of 5μm at the crossing are implemented to reduce the crossing loss [8], [33]. The radius for the large-angle bending is 50 μm. The main structure parameters for the NLC-core waveguide pattern are summarized in Table 1.

As shown in Fig. 5(a), the overall electrode pattern covers the portions of both the 1 $\times$ 2 switching element and the NLC-core waveguide. The black dash box indicates the electrodes for one unit cell, and those outside the box belong to the adjacent unit cells. From the function's point view, the overall electrode pattern can be divided into two branches, one for the lead-in/lead-out process and the other for the bending process. The electrodes covering the NLC-core waveguide are wider than the polymer channel, with the width (W_{NLC} in Fig. 5(a)) as 8 μm. The gap between the electrodes in the adjacent unit cells is 0.5 μm (with consideration of the 0.35 μm CMOS technology [30], [34]). It is noted that the electrode gap on the right-bottom side is located near the end of the waveguide taper, with the position between the ends of 90-degree bending electrode and the narrow NLC-core waveguide (Fig. 4). An electrode gap (W_g in Fig. 5(a)) of 2 μm is used at the location of 90-degree bending electrode for electrical isolation.

As for switching, one of the two branches is turned on by applying the operating voltage (5 V) to the corresponding electrode while the other one is turned off by applying 0 V, whose ports are denoted by V_{s1} and V_{s2} in Fig. 5(a), respectively. The 90-degree bending electrode is constantly driven by the operating voltage of 5V (port with V_{cc} in Fig. 5(a)). The electrode pattern for the 1 $\times$ 2 switching element is further depicted in Fig. 5(b), and it can be seen that the driving electrodes is symmetric and composed of three branches. Each of the bending branches consists of two arcs, which have the same bending radius and are tangential to each other at the junction.

The important structural parameters of the electrode pattern include the bending radius R, the bending angle α, the gap G_b between the bending branches, the gap G_s between the bending branches and the straight branch, the width W_b of each bending branch, and the width W_s of straight branch. For simplification, here we take $G_b = G_s$ and $W_s = 2W_b + G_b$. The major design parameters are summarized in Table 2.

In order to keep the NLC at nematic phase, it is essential to control the working temperature of the device below 25 °C [20]. The driving voltage is 5 V alternative-current (AC) sinusoidal wave with the frequency of 1 kHz in order to counteract the ion transport [35], and to eliminate the electrolyzing effects and the possible electro-hydrodynamics (EHD) instabilities [16].

TABLE 2
Major Design Parameters of the Switching Structure

Parameters	Values
LC chamber thickness T_{LC}	4 μm
LC alignment layer thickness T_{SiO}	100 nm
Bending branch width W_b	1 μm
Bending branch gap G_b	0.5 μm
Straight branch width W_s	2.5 μm
Bending/straight branch gap G_s	0.5 μm
Bending radius R	216 μm
Bending angle α	11.6°

TABLE 3
Properties of the Materials Used in the Proposed Device

Material	Permittivity (1 kHz)	Permittivity (optical frequency)	Others
E7 (Merck)	5.3 (⊥), 18.6 (//)	Ref. 36, Ref. 37 (e.g. 1.70 (e), 1.50 (o) @ 1550nm)	*Elastic constants* K_{11} = 10.3 pN, K_{22} = 7.4 pN, K_{33} = 16.48 pN [20]
Al	–	Ref. 38	–
SiO_2	3.91	Ref. 39 (e.g. 1.44 @ 1550nm)	–

4. Numerical Simulations and Analyses

4.1 Simulations Method

Numerical simulations are conducted to evaluate the sample design's light propagation and loss performance by the bottom-up method for approximation [27].

In the simulations, the configuration of the NLC (the orientation angles θ and ϕ *of* the directors) is firstly calculated using the weak-form partial differential equation (PDE) solver in COMSOL. Based on the calculated NLC director and the corresponding permittivity distribution, the light field propagation is then simulated by using COMSOL or FDTD (Lumerical FDTD Solution). Particularly, the calculation of NLC configuration is based on the Oseen-Frank continuum elastic theory [20], [24], and the minimization of the total free energy. Besides the free-energy minimization, it is also essential to consider the coupling between the electric field and the NLC director configuration [33], which is resolved by an iteration scheme of segregated electric field – NLC director calculations.

For the materials involved in the sample device, their main properties are summarized in Table 3. As an approximation, the permittivity of the alignment layer (SiO_x) is assumed to be the same as SiO_2. As for the polymer in NLC-core waveguide element, the permittivity is assumed as isotropic ($\varepsilon_\perp$) for both the low frequency and the optical frequency. In the simulations using the FDTD solution, the RI models of aluminum and SiO_2 are taken from Palik [40]. The default central wavelength is chosen as 1550 nm through the simulations.

The loss performance is divided into two factors including the absorption loss (from the electrodes) and the propagation loss (from the waveguide). Both of them are evaluated from 2D simulations, considering the transverse cross-section (XZ plane in Fig. 3), and the lateral cross-section (XY plane in Fig. 4), respectively.

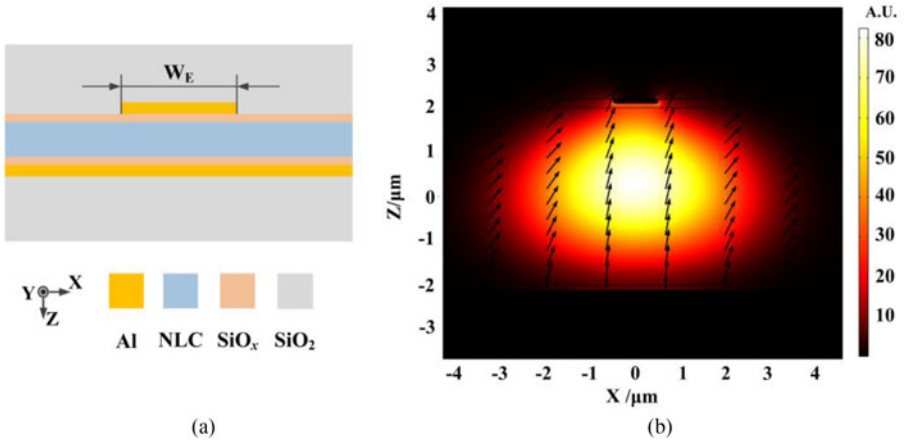

Fig. 6. (a) 2D model with the definition of the electrode width W_E and (b) The fundamental mode for $W_E = 1\ \mu$m.

For the absorption loss, both the NLC configuration and the light propagation are calculated through 2D model, and both the NLC EO waveguide and the NLC-core waveguide are considered. In contrast, the NLC calculations are performed in 3D model for more accurate propagation loss evaluation. The light propagation is firstly simulated in 1 $\times$ 2 switching element, and then the more complicated single unit cell.

4.2 Simulations on Transverse Cross-Section (XZ Plane)

4.2.1 NLC EO Waveguide: As for NLC EO waveguide, the 2D model is sketched in Fig. 6(a), with the definition of the electrode width W_E. The CMOS layer is neglected for simplification, and the operating voltage is directly applied to the driving electrodes.

In the simulations, the typical electrode width W_E of 1 μm is considered (see bending branch width in Table 2). The fundamental mode field (Z polarization component) is presented in Fig. 6(b). It is seen that the electrode with a finite width confines the electric field and thus the mode field in the X direction. The effective RI of the fundamental mode is $1.669198 - \mathbf{i}5.05284 \times 10^{-5}$, and the corresponding absorption loss is thus 1.8 dB/mm. For the other three high-order modes, their absorption losses are found to be several orders higher than that of the fundamental mode, and they are quickly attenuated during the propagation.

It is noted that the fundamental mode field is not purely Z polarized (black arrows in Fig. 6(b) indicating the polarization). The polarization perturbation at the boundary degrades the confinement of the waveguide, especially at the sharp bend.

4.2.2 NLC-Core Waveguide: Similarly, the absorption loss in NLC-core waveguide is estimated. In the NLC-core waveguide, the NLC inside the channels is driven by a constant operating voltage, and the polymer always serves the cladding (see part III in Fig. 1(c) or Fig. 4). The electrodes in this portion cover the whole channels. From the simulations, the absoprtion loss is about 0.8 dB/mm for the channel width W_C of 5 μm, and it becomes 1.2 dB/mm for $W_C = 1\ \mu$m. It is found that the variation in permittivity of the polymer has a mild effect on the absorption loss and is thus can be neglected.

4.3 The 1 x 2 Switching Element

The 1 $\times$ 2 switching element is the key part for switching function, and its performance will be simulated and analyzed, with the layered structure in Fig. 3, the electrode pattern in Fig. 5, and the

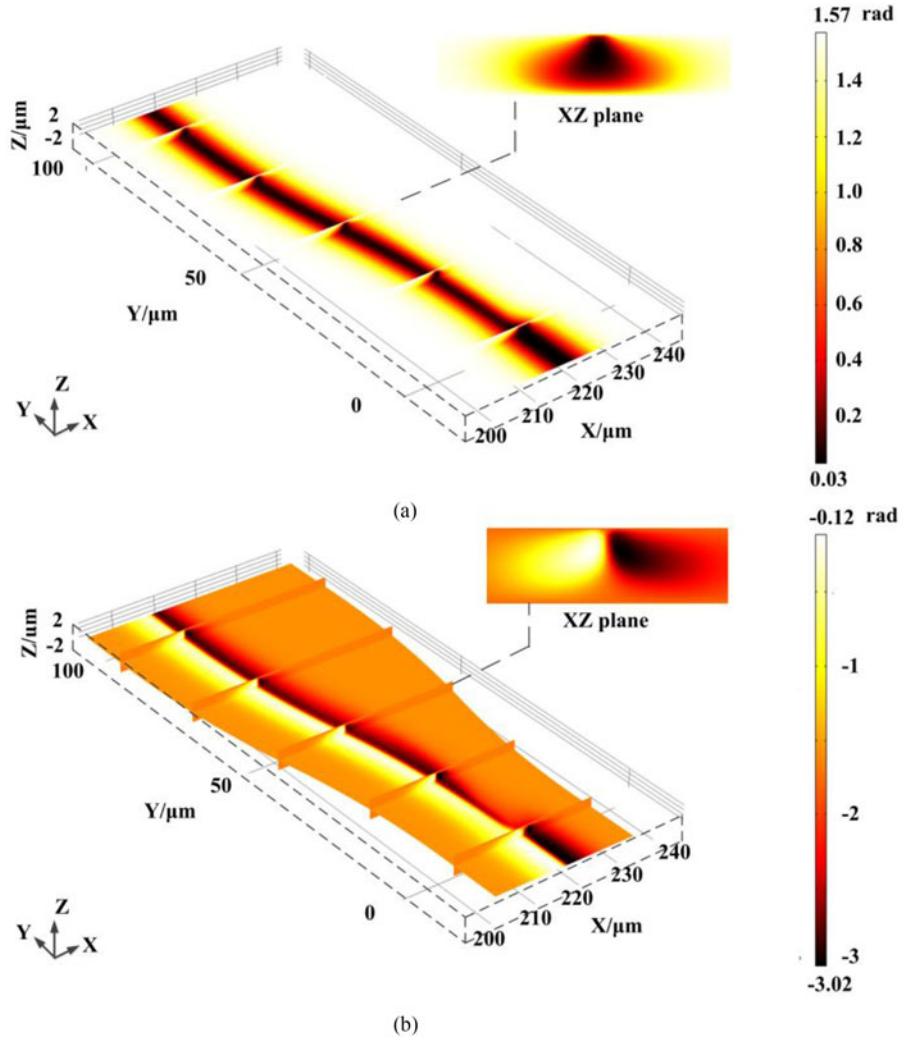

Fig. 7. Simulated 3D distributions of the orientation angles are shown, with (a) the tilt angle θ and (b) the twist angle ϕ. The insets show the enlarged views in the XZ plane.

major design parameters listed in Table 2. The origin (with X = 0 and Y = 0) is chosen at the center of the first arc in the upper bending branch (see Fig. 7).

For the considered operation, the straight branch and one of the bending branches are applied with high operating voltage (5 V as aforementioned), while the other bending branch is under zero operating voltage. The results for the other switching path can be directly inferred based on the structure symmetry.

4.3.1 3D NLC Director Configuration: At the first step, the 3D NLC director configuration under certain electric control is calculated. The NLC is commonly modeled as the composite of rod-like molecule, and the NLC E7 in the NLC-OXC is uniaxial [20], [24]. The orientation of the molecule director **n** can be defined in the cylindrical coordinate, by the tilt angle θ (between **n** and the Z-axis) and the twist angle φ (in the plane perpendicular to the Z-axis).

The 3D distribution of the orientation angles θ and ϕ are presented in Fig. 7(a) and (b), respectively. The particular cross-sectional views are shown, including the XY cross-section locating at Z = 0, and the XZ cross-section at a typical Y position (indicated by the dash line).

As seen from the XY cross-section views, the NLC directors are reoriented in the region of high-voltage electrodes, and remain pre-aligned in the other portions. The NLC directors between

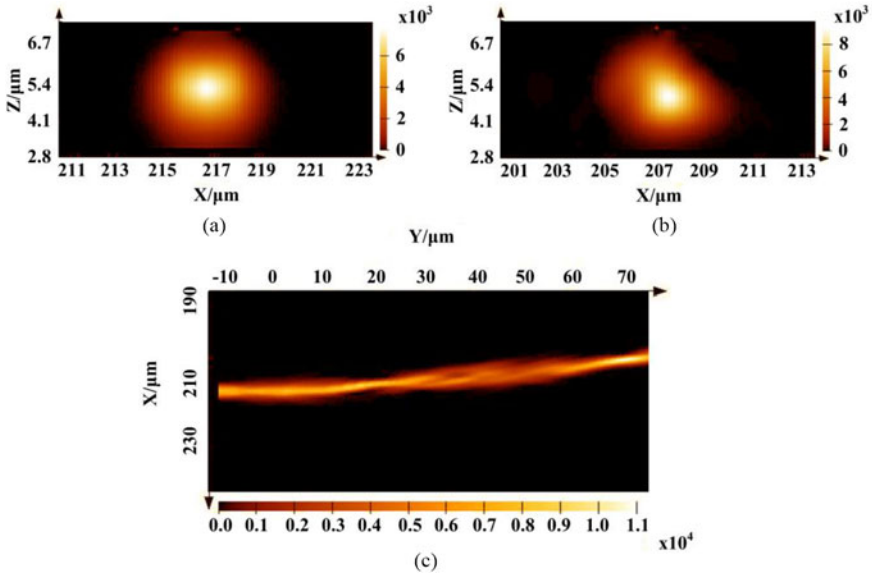

Fig. 8. The light fields (Z-polarization component) are shown at (a) the input and (b) the output location. (c) The propagation light field (Z-polarization component) is shown on the central cut plane of the NLC chamber.

the gap of straight branch and the selected bending branch are also reoriented, thanks to the fringing-field effect. Consequently, the width of NLC reorientation region changes smoothly at the junction, though the straight branch is twice wider than the bending one.

From the XZ cross-section views, it is further seen that the NLC directors have a gradient distribution. The orientation angle ϕ has an anti-symmetric gradient distribution, which is mainly due to the X component of electric field at the edge of the electrodes. There is no abrupt change of ϕ, which varies gradually as $-\pi/2 \rightarrow 0 \rightarrow -\pi/2 \rightarrow -\pi \rightarrow -\pi/2$, from left to right along the X direction. It implies the stable distribution of the NLC.

4.3.2 3D Light Propagation Simulations: The light propagation is then calculated and verified by the 3D simulations using the FDTD solutions.

The light source used in the simulations is the same as the straight NLC-core waveguide in the lead-in (see part I in Fig. 1(c)), with the width $W_i = 5\,\mu$m (the same as W_C in Table 1). The light fields (Z-polarization component) at the input and output locations are presented in Fig. 8(a) and (b), while the propagation light field (Z-polarization component) in the central cut plane of the NLC chamber is presented in Fig. 8(c). The input location is 2 μm from the source, and the output location is Y $= 74\,\mu$m, which helps achieve stable computation at the sacrifice of a little bit of accuracy. Comparing the output mode field to the input one, it is seen there is distortion at the upper-right corner, mainly due to the asymmetric bend structure.

The propagation loss is evaluated by comparing the powers of the input and the output light fields. Within the bucket centered at X $= 207.177\,\mu$m and of width 4 μm, the power of Z-polarization light field at the output location is about 0.88 of the power of light field in the cross-section at the input location. The total power of light field across the cross-section is around 0.93, which implies that the power proportion of the Z-polarization component is approximately 0.95. It is noted that the calculation accuracy is also limited by the meshing density under the available memory.

In the device design and optimization phase, it provides higher efficiency to perform a 2D light propagation simulation instead of the direct 3D one. The light propagation is also calculated in the 2D lateral cross-section (XY plane). The propagation light fields of the three polarization components are mapped, which are consistent with the above 3D simulations (not shown here for the succinct illustrations). It can be observed that there is a transfer between the Z polarization and the other two polarization components, and vice versa. It is thus possible to find out an optimal output position,

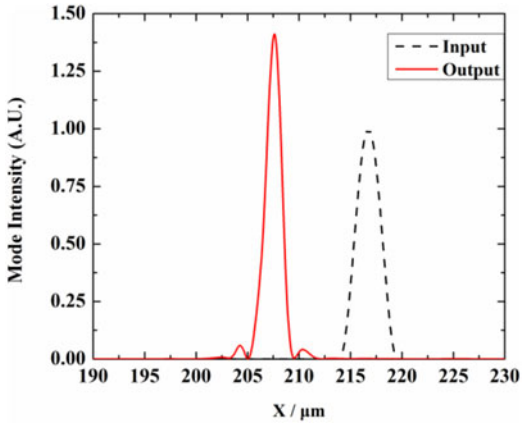

Fig. 9. The Z polarization components of the mode fields at Y = 75μm (solid line) and at the input (dash line).

balancing the trade-offs among the Z polarization proportion, the propagation loss (propagation length), and the channel cross-talk (output ports' separation). By quickly sweeping the structural parameters (e.g., bending radius R and bending angle α) in the 2D simulation process, it is found that the optimal output position locates at Y = 75 μm.

At this position with Y = 75 μm, the Z polarization component of mode field is shown in Fig. 9. For comparison, the mode field at the input position is also presented. It can be seen that the mode field is close to the fundamental mode in shape, but has two small side-lobes. The output power is found to be about 0.93 of the input power. The output mode field is compressed in the X direction, and its peak intensity is larger than the input one's. The center of the output mode is at about X = 207 μm, which is 9 μm away from the center of the input mode (X = 216 μm). The light goes to the direction opposite to the non-triggered bending branch. There is almost no overlap between the output mode fields at different branches. The consistency between the 3D and the 2D simulations is thus confirmed.

4.4 Single Unit Cell

The single unit cell is evaluated in the further simulations. The propagation loss is characterized for the three propagation processes, the lead-in, the bending and the lead-out process. The light propagation is calculated in the 2D model (XY plane).

The propagation fields (Z polarization component) for each of the processes are presented in Fig. 10. As for either the lead-in process (Fig. 10(a)) or the bending process (Fig. 10(b)), the input light is injected from the lead-in waveguide in the previous unit. The light goes through the 1 $\times$ 2 switching element and is then routed to the port corresponding to the lead-in or the bending waveguide in the NLC-core waveguide element. It is noted that in Fig. 10(b) the light propagation through the 1 $\times$ 2 switching element is only partially shown. As for the lead-out process (Fig. 10(c)), the input light is injected from NLC-core waveguide of the upward unit cell. For each process, the input mode field is assumed as the perfect fundamental mode.

From Fig. 10(a), it can be seen that the narrow waveguide is important to keep the mode field nearly a fundamental mode and to achieve a low loss. Similarly, the narrow waveguide is applied in the bending process. The tapers with asymmetric structure are used at the outputs of 1 $\times$ 2 switching element, which not only collect the light as much as possible but also reshape the wide mode field into a narrow one with small distortion. As for the lead-out process and the bending process, the Y junction with special geometry is designed to combine the input light from different ports into the same output.

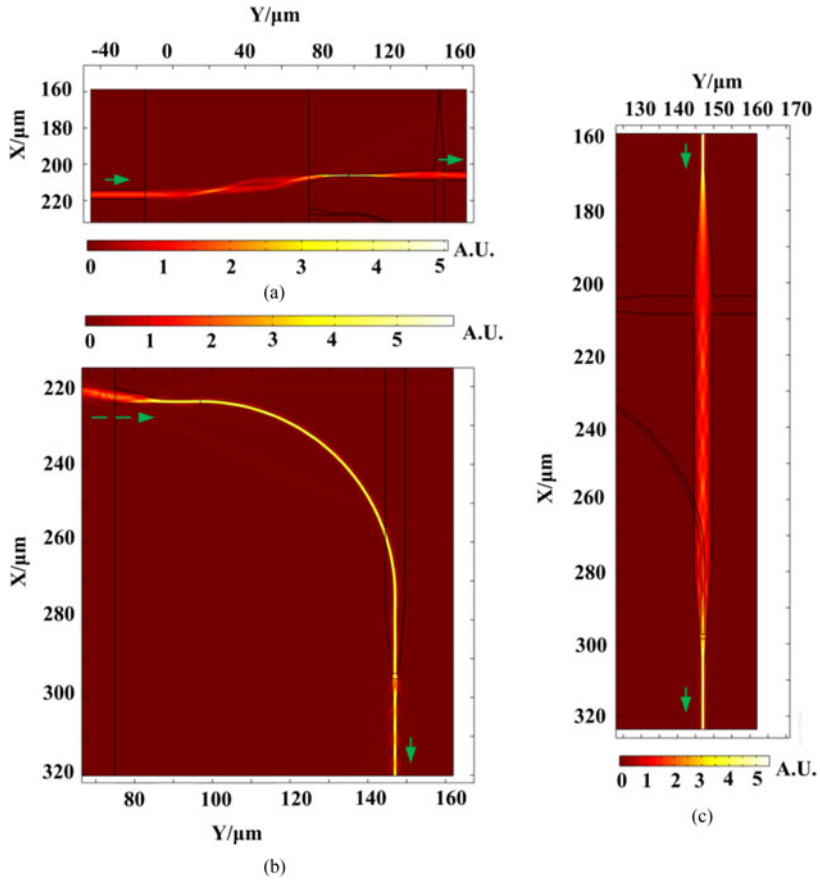

Fig. 10. The propagation light fields (Z polarization component) are shown for (a) the lead-in process, (b) the bending process and (c) the lead-out process.

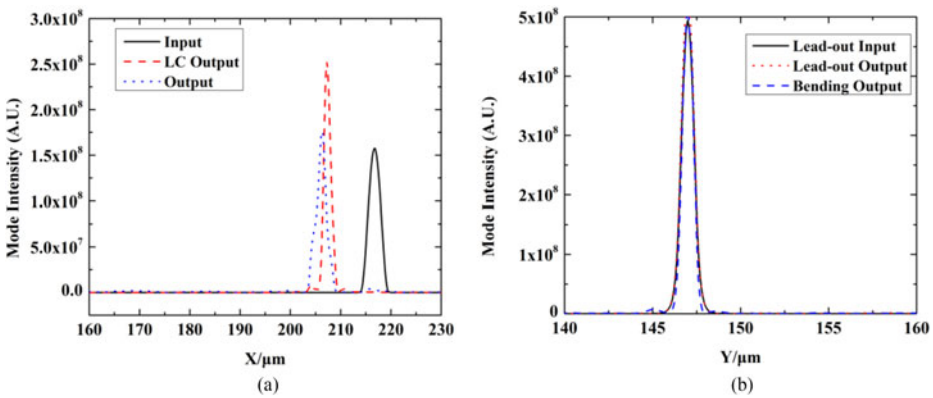

Fig. 11. The mode fields (Z polarization component) are shown for the three propagation processes, including (a) the lead-in, (b) the bending and (c) the lead-out process.

The mode fields (Z polarization component) for the three propagation states at the corresponding input/output ports are also plotted in Fig. 11. For easy comparison to the previous simulations, the mode field at the output position of 1 $\times$ 2 switching element (named as LC Output) is also shown in Fig. 11(a). It can be seen that the output mode fields are approximately fundamental mode for the three processes. It is noted that the slight distortion can be well corrected with an additional S-shape bending, which is not shown here. With large radius and small angle, the induced propagation loss

TABLE 4
The Loss Components of the Proposed Design (@1550 nm)

Parameters	When T_{LC} = 4 μm
Lead-in loss $T_{Lead\text{-}in}$	-0.45 dB
Lead-out loss $T_{Lead\text{-}out}$	-0.15 dB
Bending loss T_{Bend}	-0.51 dB
Scattering loss T_{Sca}	-0.2 dB/mm
Absorption loss in 1 × 2 switching element $T_{Abs,S}$	-1.78 dB/mm
Absorption loss in NLC-core waveguide $T_{Abs,F}$	-0.83 dB/mm

from the S-shape bending can be low enough and neglected. From Fig. 11(b), it can be seen that the center of the mode field is aligned to the input mode field, in both the lead-out process and the bending process.

At the 1550 nm wavelength, the propagation losses are around −0.45 dB, −0.51 dB, and −0.15 dB for the lead-in, the bending and the lead-out process, respectively. The cross-talks for the three propagation states are also calculated, which are −44.3 dB, −20.1 dB and −40.0 dB for the lead-in, the bending and the lead-out process, respectively. The dispersion for the propagation loss is mild in the C-band and can be neglected.

5. Performance Analyses and Discussions

5.1 Propagation Loss

Considering the electrode absorption loss (Section 4.2) and the propagation loss (Section 4.4) in the above simulations, the on-chip insertion loss for the proposed device with $N \times N$ unit cells can be estimated, with the scaling equation as follows,

$$\begin{aligned} T_{Insertion} = &[T_{Lead-in} + L_{1\times2}(T_{Abs,S} + T_{Sca}) + L_{Lead-in}(T_{Abs,F} + T_{Sca})] \times (N-1) \\ &+ [T_{Lead-out} + L_{Lead-out}(T_{Abs,F} + T_{Sca})] \times (N-1) \\ &+ (T_{Bend} + L_{1\times2}L_{Lead-in}(T_{Abs,S} + T_{Sca}) + L_{Bend}T_{Sca}), \end{aligned} \quad (1)$$

in which $T_{Lead-in}$, $T_{Lead-out}$, T_{Bend}, $T_{Abs,S}$, $T_{Abs,F}$ and T_{sca} denote the loss for the lead-in process, the lead-out process, the bending process, the absorption loss in the 1 × 2 switching element, the absorption loss in the NLC-core waveguide element and the scattering loss, respectively. The scattering loss T_{Sca} is 2 dB/cm [41]–[44] in the C-band. It is noted that the scattering light can be largely absorbed by the electrodes, with mild effect on the cross-talk. The loss components are listed in Table 4. Besides, $L_{Lead-in}$, $L_{Lead-out}$, L_{Bend} *and* $L_{1\times2}$ stand for the length of propagation path in the lead-in process, the lead-out process, the bending process and the 1 × 2 switching element, respectively. It is estimated that $L_{1\times2} = 90\,\mu$m, $L_{Lead-in} = 90\,\mu$m, $L_{Lead-out} = 165\,\mu$m and $L_{Bend} \approx 200\,\mu$m, as summarized in Table 1.

Based on Eq. (1), the maximum on-chip insertion loss for different numbers of unit cells is estimated as plotted in Fig. 12. It can be seen that the on-chip insertion loss increases linearly with the number of unit cells. For the sample design, the minimum and the maximum on-chip insertion loss for the 8 × 8 OXC is estimated to be 0.7 dB and 8.0 dB, with the difference of about 7.3 dB.

Some potential methods can be used to further reduce the on-chip insertion loss. The first method is to use a thicker NLC chamber at the cost of a longer switching time. Another method for the loss reduction is to increase the thickness of SiO_x (or additional SiO_2 above the electrode) layer, which can suppress the absorption of the electrodes. However, the operating voltage should be raised to achieve stable NLC reorientation. A possible configuration is to use SiO_x layer of 100 nm with an additional SiO_2 layer of 200 nm above the electrode in structure. The corresponding operating

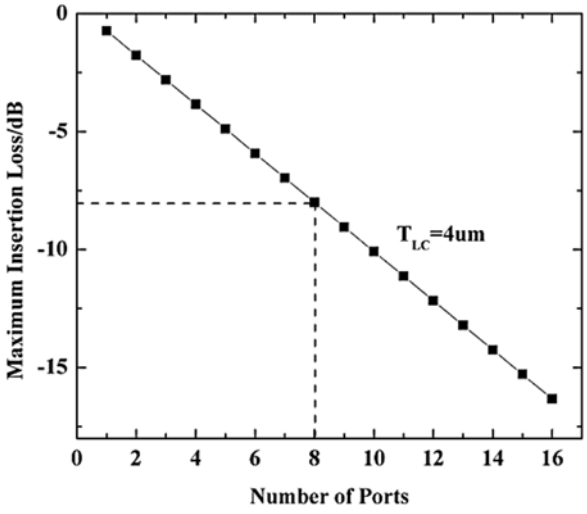

Fig. 12. Maximum on-chip insertion loss is plotted for different number of input ports.

voltage is 6.5 V to maintain a similar propagation feld in the 1×2 switching element. It can be found that the absorption loss due to the electrode is thus reduced to about 0.25 dB/mm (with the effective RI as $1.675713 - \mathbf{i}7.067217 \times 10^{-6}$) for $T_{Abs,S}$. The maximum total insertion loss for this configuration is estimated to be about 5.5 dB for the 8×8 blocks according to Eq. (1).

It can also be seen that the dispersion is low for the propagation loss, with the maximum variation of about 0.2 dB across the C-band in the 8×8 OXC. The broadband property is due to non-resonant waveguide structures and the low dispersion in the selected materials.

5.2 Cross-Talk

Similarly, the cross-talk can also be estimated for the 8×8 block in the proposed device [4]. From the simulations above, the cross-talks in the unit cell are about -44.3 dB, -20.1 dB and -40.0 dB for the lead-in, the bending and the lead-out process, respectively. With the cross-talks in the unit cell, the signal-to-cross-talk ratio SXR [4] can be estimated as $-X_{Lead-in} - 10\log_{10}(N-1)$, and $-X_{Bend} - X_{Lead-in} - 10\log_{10}(N-1)$, in the worst case ($I_N$ to O_1) and the best case (I_1 to O_N), respectively. Here X is the cross-talk in each unit cell. For the 8×8 OXC, an average cross-talk is achieved down to -45.9 dB. The worst and the best cross-talks are estimated to be -35.8 dB and -55.9 dB, respectively.

5.3 Switching Speed

The NLC-OXC is also limited by the slow switching time (off-time), which is at the order of tens of milliseconds. When $T_{LC} = 4\ \mu$m, the switching time can be estimated as about 16 ms [45]. There are some possible methods to speed up the switching, as reported in the studies in the LCD technology. The overdriving scheme and the NLC material are the two common methods [46]. Recently, the 3-T electrode structure was proposed to shorten the switching off time to sub-millisecond [46]. With the similar electrode structure and the alignment remaining, it is possible to use additional electric field to drag the NLC molecule, and helps speed up the switching off process to about 1 ms.

5.4 Coupling Interface

Another important practical issue is the fiber-to-chip coupling. To achieve the polarization-dependent routing in the NLC-OXC, the coupled light wave to the access waveguide should be preprocessed

to be the transverse-magnetic (TM) mode. The polarization-independent coupling is also preferred, since the polarization state is dynamically randomly-varying in the real optical communication systems. This issue is common in the silicon photonic and nano-photonic waveguides in photonic integrated circuit [47], [48]. Using the current techniques [47]–[52], several potential solutions can be found to address the polarization issue in NLC-OXC.

The polarization-independent grating coupler can be used as the fiber-to-chip interface. In the state of the art of grating couplers, the coupling efficiency exceeds 50%, and the available bandwidth covers the whole C-band, with typically length about a hundred μm [48], [49]. The polarization diversity can be adopted [50], in which two copies of the NLC-OXC are implemented for processing the transverse-electric (TE) and the TM mode, respectively.

In the end-coupling, it is also effective to use polarization maintaining fiber (PMF) at the interface with accurate pre-alignment packaging [51]. The polarization diversity method can be adopted using the integrated polarization converter [47] in front of the input port, or using the fiber-based beam polarization splitters/combiners [52].

5.5 Fabrication Issue

As for the sample device, it can leverage on the LCD/LCoS fabrication technology [20], [30], and [34], especially for the CMOS layer and topmost the electrode pads. As aforementioned, the alignment layer of SiO_x is applied, for which the deposition method can be adopted [31], [32]. It is thus free of rubbing process and compatible with CMOS fabrication technology. However, the patterning for NLC chamber layer makes the fabrication tougher than the conventional LCD/LCoS devices. For the polymer channel, the fabrication can be developed from the microfluidic/optofluidic devices [22]. The NLC-core waveguides have been experimentally demonstrated with the polymer cladding [21], [23], which also provides helpful experiences in the fabrication of the proposed device. The registration between the polymer channel and the corresponding electrode pad is expected to be controlled by the mature techniques in the standard lithography.

6. Conclusions

In conclusions, a planar OXC switch (NLC-OXC) is proposed using the EO waveguides in NLC. The NLC-OXC employs the cross-bar fabric and consists of an array of unit cells that are switched by NLC EO waveguides. The NLC-core waveguides surrounded by the polymer claddings further define and support beam routing paths for the lead-in/lead-out processes or the bending process. Different from the previous NLC waveguide devices, the NLC EO waveguides and the NLC-core waveguides are combined into the hybrid structures in the proposed device, which enables better integration and performance in the matrix of switching units. It has the layered structure similar to the LCoS, and can leverage the fabrication techniques of the LCD/LCoS.

With the revelation of the important physical properties in NLC waveguides, the device is designed, analyzed and simulated using the bottom-up method. The structure parameters are selected and determined by theoretical analyses and numerical simulations. The sample design presents an 8×8 NLC OXC with the NLC chamber thickness $T_{LC} = 4\,\mu$m. The NLC EO waveguide can be switched on by the 5 V-1 kHz sinusoidal-wave voltage. It exhibits a maximum on-chip insertion loss of around 8.0 dB, a switching time of 16 ms, a footprint of 2 mm $\times$ 2 mm, and a cross-talk of about -45.9 dB in total. Using a higher operating voltage of 6.5 V and a 300-nm SiO_x insulator layer above the electrodes, the maximum on-chip insertion loss can be reduced to about 5.5 dB. With additional 3-T electrodes for turn-off driving, the shorter switching time of about 1 ms can be achieved. It can operate at broad bandwidth with the maximum insertion loss variation of around 0.2 dB across C-band.

The proposed NLC-OXC is expected to enjoy the advantages of both the LCoS and the planar waveguide in the aspects of compactness, robustness, power consumption and also optical loss. It is promising for robust optical circuit switching in small-scale data centers, or protection switching in optical communication networks.

References

[1] C. Kachris, K. Kanonakis, and I. Tomkos, "Optical interconnection networks in data centers: Recent trends and future challenges," *IEEE Commun. Mag.*, vol. 51, no. 9, pp. 39–45, Sep. 2013.

[2] G. Wang *et al.*, "Your data center is a router: The case for reconfigurable optical circuit switched paths," in *Proc. ACM HotNets-VIII*, 2009, pp. 1–6.

[3] K. Chen *et al.*, "OSA: An optical switching architecture for data center networks with unprecedented flexibility," *IEEE/ACM Trans. Netw.*, vol. 22, no. 2, pp. 498–511, Apr. 2014.

[4] T. S. El-Bawab, *Optical Switching*. New York. NY, USA: Springer, 2006, pp. 1–32.

[5] J. Kim *et al.*, "1100 × 1100 port mems-based optical crossconnect with 4-db maximum loss," *IEEE Photon. Technol. Lett.*, vol. 15, no. 11, pp. 1537–1539, Nov. 2003.

[6] G. Baxter *et al.*, "Highly programmable wavelength selective switch based on liquid crystal on silicon switching elements," in *Proc. Opt. Fiber Commun. Conf. Nat. Fiber Optic Eng. Conf.*, 2006, pp. 1–3.

[7] Q. Cheng, M. Ding, A. Wonfor, J. Wei, R. V. Penty, and I. H. White, "The feasibility of building a 64 × 64 port count SOA-based optical switch," in *Proc. Int. Conf. Photon. Switching*, 2015, pp. 199–201.

[8] L. Chen and Y. Chen, "Compact, low-loss and low-power 8 × 8 broadband silicon optical switch," *Opt. Exp.*, vol. 20, pp. 18977–18985, 2012.

[9] S. Han, T. J. Seok, N. Quack, B. Yoo, and M. C. Wu, "Monolithic 50 × 50 mems silicon photonic switches with microsecond response time," in *Proc. Opt. Fiber Commun. Conf. Nat. Fiber Optic Eng. Conf.*, 2014, pp. 1–3.

[10] Y. Kai, K. Sone, S. Yoshida, Y. Aoki, G. Nakagawa, and S. Kinoshita, "A compact and lossless 8 × 8 SOA gate switch subsystem for WDM optical packet interconnections," in *Proc. 34th Eur. Conf. Opt. Commun.*, 2008, pp. 1–2.

[11] I. Szcesniak, "Overview of optical packet switching," *Theoretical Appl. Informat.*, vol. 21, pp. 167–180, 2009.

[12] H. Toshiyoshi, "MEMS for micro optics: from fiber optic communication to display," in *Proc. SPIE*, 2005, vol. 6050, pp. 605007-1–605007-6.

[13] Z. Zhang, Z. You, and D. Chu, "Fundamentals of phase-only liquid crystal on silicon, LCOS devices," *Light Sci. Appl.*, vol. 3, pp. 1–10, 2014.

[14] Y. Zuta, I. Goykhman, B. Desiatov, and U. Levy, "On-chip switching of a silicon nitride micro-ring resonator based on digital microfluidics platform," *Opt. Exp.*, vol. 18, pp. 24762–24769, 2010.

[15] A. Pyayt, J. Luo, A. K.-Y. Jen, L. Dalton, and A. Chen, "Field-induced guiding optical devices made from electro-optic polymers," *Appl. Opt.*, vol. 49, pp. 892–896, 2010.

[16] A. G. Maksimochkin, S. V. Pasechnik, G. I. Maksimochkin, and V. G. Chigrinov, "Electrically controlled waveguide mode in LC layer for fiber optic applications," *Opt. Commun.*, vol. 283, pp. 3136–3141, 2010.

[17] F. Costache and M. Blasl, "Optical switching with isotropic liquid crystals: Towards easily integrable electro-optical waveguide switching technology," *Optik Photonik*, vol. 6, pp. 29–31, 2011.

[18] M. Blasl, K. Bornhorst, and F. Costache, "Polarization insensitive variable optical attenuator based on field induced waveguides with a liquid crystal core," in *Proc. Opt. Fiber Commun. Conf. Nat. Fiber Optic Eng. Conf.*, 2015, pp. 1–3.

[19] F. Costache, H. Hartwig, K. Bornhorst, and M. Blasl, "Variable optical power splitter with field-induced waveguides in liquid crystals in paranematic phase," in *Proc. Opt. Fiber Commun. Conf. Nat. Fiber Optic Eng. Conf.*, 2014, pp. 1–3.

[20] D. K. Yang and S. T. Wu, *Fundmentals of Liquid Crystal Devices*. Chichester, U.K.: Wiley, 2015, pp. 1–285.

[21] T.-J. Wang, C.-K. Chaung, W.-J. Li, T.-J. Chen, and B.-Y. Chen, "Electrically tunable liquid-crystal-core optical channel waveguide," *J. Lightw. Technol.*, vol. 31, no. 22, pp. 3570–3574, Nov. 2013.

[22] A. d'Alessandro, L. Martini, G. Gilardi, R. Beccherelli, and R. Asquini, "Polarization-independent nematic liquid crystal waveguides for optofluidic applications," *IEEE Photon. Technol. Lett.*, vol. 27, no. 16, pp. 1709–1712, Aug. 2015.

[23] M. Sharma, M. R. Shenoy, and A. Sinha, "Low-loss optical switch using liquid crystal core waveguide with polymer cladding," *J. Lightw. Technol.*, vol. 34, no. 13, pp. 3065–3070, Jul. 2016.

[24] D. Donisi, R. Asquini, A. d'Alessandro, and G. Assanto, "Distributed feedback grating in liquid crystal waveguide: A novel approach," *Opt. Exp.*, vol. 17, pp. 5251–5256, 2009.

[25] D. C. Zografopoulos and R. Beccherelli, "Design of a vertically coupled liquid-crystal long-range plasmonic optical switch," *Appl. Phys. Lett.*, vol. 102, 2013, Art. no. 101103.

[26] K.-H. Fan-Chiang, S.-T. Wu, and S.-H. Chen, "Fringing-field effects on high-resolution liquid crystal microdisplays," *J. Display Technol.*, vol. 1, pp. 304–313, 2005.

[27] L. Chrostowski, *Silicon Photonics Design*. London, U.K.: Cambridge Univ. Press, 2015, pp. 1–414.

[28] I.-C. Khoo, *Liquid Crystals*. Hoboken, NJ, USA: Wiley, 2007, pp. 1–190.

[29] M. L. Jepsen, "Liquid crystal on silicon," *Nat. Photon.*, vol. 1, pp. 276–277, 2007.

[30] W. P. Bleha, L. Juan, and A. Lei, "Advances in liquid crystal on silicon, lcos spatial light modulator technology," in *Proc. SPIE*, 2013, vol. 8736, pp. 87360A-1–87360A-7.

[31] P. K. Son, J. H. Park, J. C. Kim, and T.-H. Yoon, "Control of liquid crystal alignment by deposition of silicon oxide thin film," *Thin Solid Films*, vol. 515, pp. 3102–3106, 2007.

[32] L. De Sio, A. E. Vasdekis, J. G. Cuennet, A. De Luca, A. Pane, and D. Psaltis, "Silicon oxide deposition for enhanced optical switching in polydimethylsiloxane-liquid crystal hybrids," *Opt. Exp.*, vol. 23, pp. 23532–23537, 2011.

[33] Y. Fu, T. Ye, W. Tang, and T. Chu, "Efficient adiabatic silicon-on-insulator waveguide taper," *Photon. Res.*, vol. 2, pp. A41–A44, 2014.

[34] J. Szentesi and T. Balogh, "State of the art in LCOS," 2004, pp. 1–31. [Online]. Available: http://holovision project.holografika.eu/news_files/60_53.2_2 State-of-the-art in LCOS_public, Holovision Project.

[35] K. Neyts and F. Beunis, "Ion transport in liquid crystal," in *Handbook of Liquid Crystal,* 2nd ed., vol. 2, J. W. G. Goodby, Ed. Weinheim, Germany: Wiley-VCH Verlag, 2014.

[36] A. K. Pitilakis, D. C. Zografopoulos, and E. E. Kriezis, "In-line polarization controller based on liquid-crystal photonic crystal fibers," *J. Lightw. Technol.*, vol. 29, no. 17, pp. 2560–2569, Sep. 2011.

[37] J. Li, S.-T. Wu, S. Brugioni, R. Meucci, and S. Faetti, "Infrared refractive indices of liquid crystals," *J. Appl. Phys.*, vol. 97, 2005, Art. no. 073501.
[38] A. D. Rakic, A. B. Djurisic, J. M. Elazar, and M. L. Majewski, "Optical properties of metallic films for vertical-cavity optoelectronic devices," *Appl. Opt.*, vol. 37, pp. 5271–5283, 1998.
[39] H. Malitson, "Interspecimen comparison of the refractive index of fused silica," *J. Opt. Soc. Am.*, vol. 55, pp. 1205–1208, 1965.
[40] E. D. Palik, *Handbook of Optical Constants of Solids*. Boston, MA, USA: Academic, 1985.
[41] D. Hermann, "Integrated optics with liquid crystals," Chalmers Univ. Technol., Goteberg, Sweden, 2000, pp. 1–33. [Online]. Available: http://fy.chalmers.se/-f9adh/pub/LCIO-Hermann.pdf
[42] S.-T. Wu and K.-C. Lim, "Absorption and scattering measurements of nematic liquid crystals," *Appl. Opt.*, vol. 26, pp. 1722–1727, 1987.
[43] S. Bolis, S.-P. Gorza, S. J. Elston, K. Neyts, P. Kockaert, and J. Beeckman, "Spatial fluctuations of optical solitons due to long-range correlated dielectric perturbations in liquid crystals," *Phys. Rev. A*, vol. 96, 2017, Art. no. 031803.
[44] M. Yoneya, Y. Utsumi, and Y. Umeda, "Depolarized light scattering from liquid crystals as a factor for black level light leakage in liquid-crystal displays," *J. Appl. Phys.*, vol. 98, 2005, Art. no. 016106.
[45] Q. Wang and S. Kumar, "Submillisecond switching of nematic liquid crystal in cells fabricated by anisotropic phase-separation of liquid crystal and polymer mixture," *Appl. Phys. Lett.*, vol. 86, 2005, Art. no. 071119.
[46] D. H. Song *et al.*, "Ultrafast switching of randomly-aligned nematic liquid crystals," *Opt. Exp.*, vol. 20, pp. 11659–11664, 2012.
[47] D. Dai and J. E. Bowers, "Novel concept for ultracompact polarization splitter-rotator based on silicon nanowires," *Opt. Exp.*, vol. 19, pp. 10940–10949, 2011.
[48] X. Chen and H. K. Tsang, "Polarization-independent grating couplers for silicon-on-insulator nanophotonic waveguides," *Opt. Lett.*, vol. 36, pp. 796–798, 2011.
[49] P. Xu *et al.*, "High-efficiency wideband SiNx-on-SOI grating coupler with low fabrication complexity," *Opt. Lett.*, vol. 42, pp. 3391–3394, 2017.
[50] W. Bogaerts, D. Taillaert, P. Dumon, D. V. Thourhout, R. Baets, and E. Pluk, "A polarization-diversity wavelength duplexer circuit in silicon-on-insulator photonic wires," *Opt. Exp.*, vol. 15, pp. 1567–1578, 2007.
[51] T. T. Aalto, M. Harjanne, and M. Kapulainen, "Method for the rotational alignment of polarization-maintaining optical fibers and waveguides," *Opt. Eng.*, vol. 42, pp. 2861–2867, 2003.
[52] Thorlabs, Fiber polarization beam combiner@1550nm, 2017. [Online]. Available: https://www.thorlabs.de.